Engineering Structures 135 (2017) 246–258

Contents lists available at ScienceDirect

Engineering Structures

journal homepage: www.elsevier.com/locate/engstruct

Compressive buckling for symmetric TWB with non-zero warping stiffness

G. Piana [a], E. Lofrano [a], A. Manuello [b,*], G. Ruta [a], A. Carpinteri [b]

[a] University "La Sapienza", Department of Structural and Geotechnical Engineering, via Eudossiana 18, 00184 Roma, Italy
[b] Politecnico di Torino, Department of Structural, Geotechnical and Building Engineering, c.so Duca d. Abruzzi, 24,10129 Torino, Italy

ARTICLE INFO

Article history:
Received 14 July 2016
Revised 19 December 2016
Accepted 20 December 2016
Available online 18 January 2017

Keywords:
Thin-walled beams
Torsion buckling
Natural frequencies
PZT sensors
Warping constraints
Numerical codes

ABSTRACT

Torsion and bending/torsion buckling may occur for compressed thin-walled open profiles used in engineering and architecture applications. We report experimental results provided by PZT pickups stuck on thin-walled aluminium beams with open modified cruciform cross-section, exhibiting non-zero warping stiffness. The buckling loads and the natural frequencies corresponding to various compressive forces were detected for free and (at least partially) restrained warping of the ends of the specimens. The results are compared with those of a FEM (commercial) and an *in-house* numerical code that examines the stability of non-trivial equilibrium paths in a dynamic setting. The results seem new and confirm that: (a) PZT pickups can be efficient in extracting modal parameters of thin-walled beams; (b) the numerical simulations are robust and accurate in finding the buckling loads in all analyzed configurations.

1. Introduction

The main feature of open thin-walled beams is high bending stiffness about at least one principal axis of inertia, but negligible torsion rigidity. The centres of area and shear are usually different, hence: bending is coupled with torsion in both the linear and nonlinear range; buckling modes are mixed; and the post-buckling behaviour is unstable [1]. In addition, their geometry makes Saint-Venant's principle not valid, and boundary effects propagate throughout the beam length [2]: thus, warping and warping constraints become appreciable, or dominant [2,3]. The numerous applications of such profiles in engineering give interest to the study of their critical load; some of the authors have published on this [4–6]. Such profiles are used, e.g., as compressed members (columns) in civil engineering: see the New National Gallery in Berlin, designed by L. Mies van der Rohe and realized between 1962 and 1968; and the New De Cecco Headquarters in Pescara (Italy), designed by M. Fuksas and realized between 2001 and 2008.

It is usually assumed that pre-buckling equilibrium paths are trivial: the load does not actually deform the member [1–3]. This is acceptable for solid beams, with high axial stiffness and negligible warping effects and bending/torsion coupling. In thin-walled beams the pre-buckling paths can affect the critical load, and studies on non-trivial equilibrium paths before buckling are interesting. The beam model in [4–6] was the basis for the studies in [7–9] by an *in-house* finite difference code. Refinements of the model are in [10], and refinements of the code are in progress, to account for full non-conservative loads.

Some of the authors, with a vast laboratory experience, studied numerically and experimentally how the natural frequencies of compressed beams vary with the load [11,12]. Indeed, in the applications the detection of this variation may be useful for design, monitoring, and damage identification. Moreover, the critical load is attained when the relevant natural frequency vanishes (ideal, perfect systems) [13–20], or is a minimum (real, imperfect systems) [11,20–24] as the load increases (i.e., the apparent beam stiffness goes down). Therefore, measures of fundamental frequency for different compressive forces can also be used for buckling load prediction through non-destructive testing [20,25–28].

An experimental campaign for open thin-walled beams was designed, aiming at: (a) generalizing the already performed experiments, to account for warping and warping constraints; (b) designing and realizing suitable end constraints to match the analytical conditions of the numerical investigation; (c) finding experimental validation of the numerical results obtained so far; and (d) highlighting, by experimental evidence, the role of pre-buckling equilibrium paths, usually neglected in the literature.

* Corresponding author.
E-mail address: amedeo.manuello@polito.it (A. Manuello).

http://dx.doi.org/10.1016/j.engstruct.2016.12.038
0141-0296/

Table 1
Geometrical and mechanical properties of the specimens.

Unconstrained length (mm)	Section width (mm)	Section thickness (mm)	Young's modulus (N m^{-2})	Poisson's ratio (–)	Mass density (kg m^{-3})
950	50	1.2 (web), 1.4 (flanges)	69×10^9	0.3	2600

The authors investigated the effect of compressive loads operated by an MTS machine on specimens constrained by end devices designed and manufactured to account for warping. The specimens were aluminium beams with symmetric cruciform section and negligible warping stiffness [1–3]. In [29] the experimental and numerical results were thoroughly described and compared. The laboratory set-up was tested, with details on the end constraints and the technique to identify natural frequencies; the *in-house* code was validated. In [11] some of us used a laser to detect the natural frequencies of beams that were slightly bent so to simulate an imperfection, or a pre-buckling path, while in [29–31] piezoelectric pickups of musical technologies were used and found to be effective, precise, robust, and reliable.

In this paper we use the same experimental setup, and new end devices designed and realized to extend the study to a new specimen with doubly symmetric cross-section of non-zero warping stiffness. Thus, we can highlight how warping and warping constraints affect the natural frequencies and buckling loads of a larger class of open thin-walled profiles. We considered two different boundary conditions on warping, and compared the results with numerical ones. The main feature of this study is the measurement of the effects of axial forces on the non-uniform torsion vibration and buckling of a symmetric open thin-walled profile: such investigations are rarely found in the literature.

2. Experimental setup

The specimens were aluminium thin-walled open profiles (6060 T5 alloy), designed and realized on purpose for the experimental campaign, the geometrical and mechanical properties of which are in Table 1. The cross-section of the specimens (see Fig. 1) has the shape of a double I, implying high bending stiffness, modest torsion stiffness, and non-negligible warping stiffness. Thus, such profiles, if not much slender, are prone to buckling more in torsion than in bending [1–3].

Fig. 2 shows the experimental setup of the tests: the loading was operated by a servo-hydraulic MTS testing machine, with a closed-loop electronic control and a maximum loading capacity of 250 kN. The specimens were vertical, constrained to the machine by connections controlling displacements, rotations and twist of the end sections. Four brass elements were designed and manufactured as end connections, so to allow the insertion of the ends of the beam and permit, or prevent (at least partially), the warping of the end sections, Fig. 3. In Fig. 3a (free warping condition) we see how the web only is constrained, while the flanges are left free. Conversely, in Fig. 3b (restrained warping), the whole section is inserted into the brass joint and both the web and the flanges are constrained. Actually, in this case penetration is prevented but detachment is allowed: thus, we have a kind of semi-restrained warping. The position of the lower joint can be adjusted in the horizontal plane so to ensure the required vertical alignment with the upper joint, Fig. 3. The tests were performed controlling the displacement of the lower end of the beam operated by the hydraulic jack, thus providing the loading.

Measures were operated by piezoelectric pickups: their features are such that very accurate dynamic identification tests can be performed without sensibly varying the specimens' mass. A PZT transducer produces an electric signal when subjected to dynamic deformation (direct piezoelectric effect), thus it does not need any supply. The signal can be amplified (if necessary), acquired by audio or usual devices, then recorded and post-processed. The sensor is stuck to the surface of the specimen by glue or a thin film of gel, and does not require specific calibration. A preliminary assessment of the capabilities of PZT disks for experimental modal analysis can be found in [30], while more accurate and complete analysis and results are reported in [31]. Further results and comparisons can be found in [29]. The main features of the adopted PZT sensor are reported in Table 2: its operating frequency range is very large and its weight is extremely low, which makes it particularly suitable for this experimental campaign.

During the tests, four PZT sensors were mounted on each specimen (their locations are marked in Fig. 2). Indeed, even though in principle one sensor is enough to detect the natural frequencies, more sensors were adopted to increase the measure redundancy.

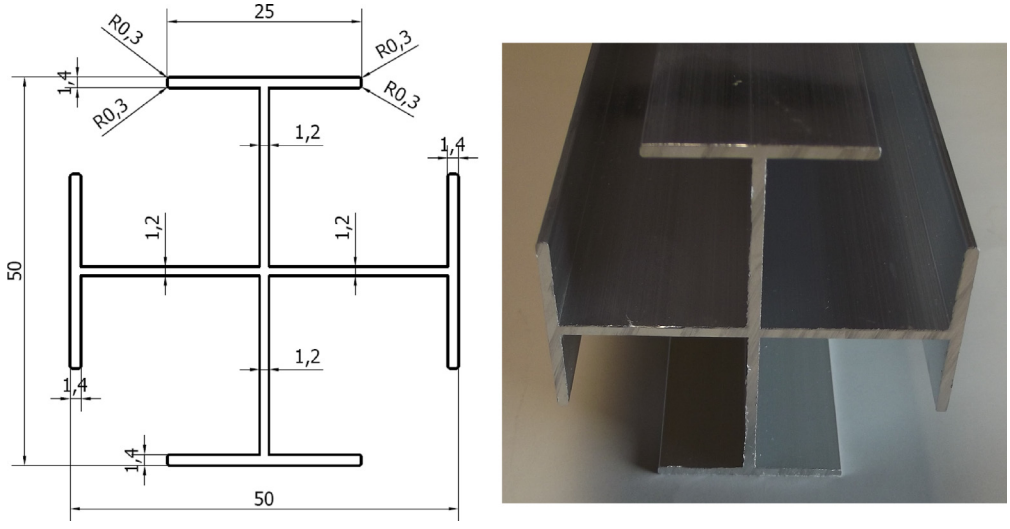

Fig. 1. Specimens cross-section: drawing (dimensions in mm) and picture.

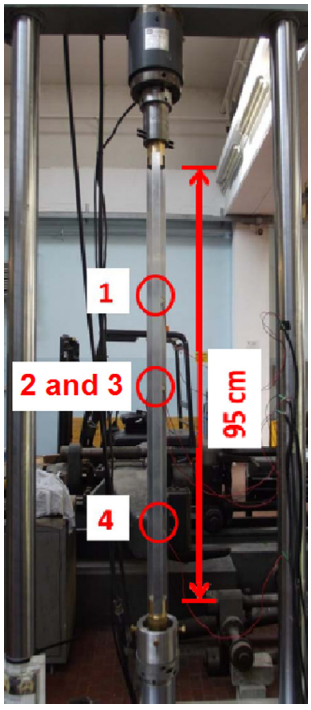

Fig. 2. Experimental setup: specimen with indication of the sensors positions.

The PZT pickups were attached to the surface of the beam web by a thin film of gel, as shown in Fig. 4.

3. Experimental tests

Apart from specimens used in preliminary stages, four beams were tested in the experimental campaign. Two kinds of tests were performed using the MTS: (i) static monotonic compression tests to determine the axial load-axial displacements curves and preliminarily detect the buckling load; and (ii) free vibration tests to identify the natural frequencies at different compression levels, up to buckling and a little beyond. Both test types (i) and (ii) were performed in the free and semi-restrained warping conditions, each time using a new, virgin sample, for a total of four tests.

The monotonic compression tests (i) were conducted operating the loading, in automatic control mode, by imposing a displacement ramp to the hydraulic jack, with a velocity of 4×10^{-6} m/s. It was then possible to measure the axial load carried by the specimen as a function of the imposed axial end displacement. The tests were stopped automatically, by specific controls activated for the post-critical branch, or, alternatively, simply by acting manually on the main software.

The dynamic tests (ii) were conducted by measuring the free vibration response through the PZT sensors at different steps of the imposed axial displacement, obtained by manually acting on the main software of the MTS. The specimen was instrumented with four pickups connected to an audio acquisition device 1818 VSL by PreSonus. Signals were processed and recorded by the software Studio One 2 by PreSonus. The signal acquisition was done at a sampling frequency of 44.1 kHz, with a resolution of 24 bits. Data post-processing was operated using *in-house* programs developed in MatLab. The procedure to extract the natural frequencies is as follows: at each loading step, the beam was excited five times by impulses transmitted to five different points located in the central part of the sample (say, between sensors 1 and 4 in Fig. 2); the corresponding signals were recorded. A non-instrumented, light hammer was used to beat the sample; the impulses were transmitted in both the web directions, usually in correspondence of flange edges to largely excite both torsion and bending vibration. A total of 20 signals (5 for each of the 4 sensors) were thus obtained for each loading step. The resonant frequencies were detected by performing the Fast Fourier Transform of the acquired signals, adopting the Peak-Picking technique [32–34]. Only the output signals were recorded during this procedure.

4. Numerical simulations

4.1. Finite element models

Finite element models were implemented in the commercial code Axis VM 12 [35], as follows: (1) free warping condition (web restrained, flanges free); (2) free warping condition (centroid restrained, rest of web and flanges free); (3) fully restrained warping.

The beams were modelled using shell elements resulting from the coupling of the 8-node Serendipity element and the 8-node Heterosis element (Fig. 5) [36]. End constraints were imposed to the nodes at the centroid; in detail, displacements and rotations were prevented at one end, whereas at the other end the longitudinal displacement was allowed, while preventing all the other degrees of freedom (Fig. 5a). Further constraints controlled warping at the end sections as follows: for restrained warping, a thin

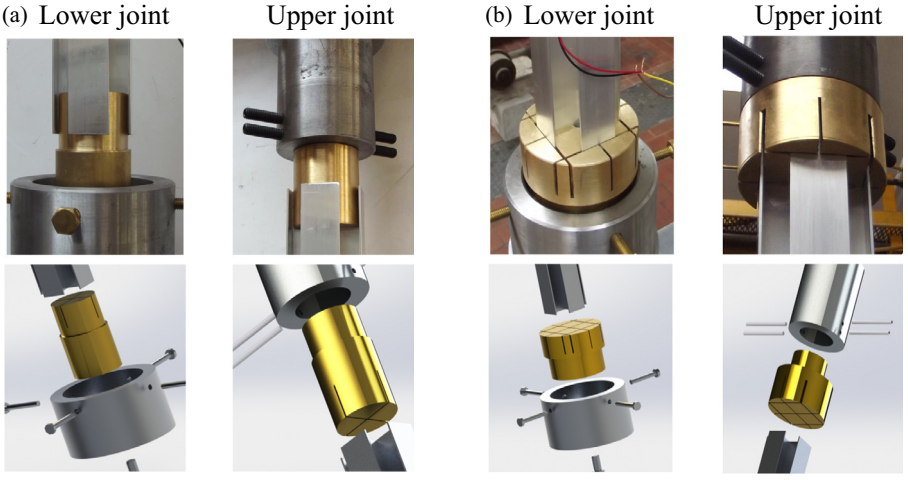

Fig. 3. Picture (*top*) and rendering (*bottom*) of end constraints: (a) lower (*left*) and upper (*right*) joint for the case of free warping, (b) the same in the case of semi-restrained warping.

Table 2
Main characteristics of the PZT sensor.

External diameter (mm)	Frequency range (kHz)	Resonant frequency (kHz)	Operating temperature (°C)	Weight (g)
20	~0 to 20	6.0 ± 0.5	−20 to +50	~1

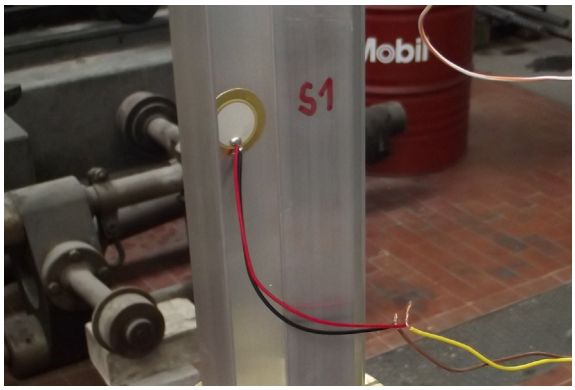

Fig. 4. PZT pickup attached to the beam web for the detection of the natural frequencies.

(1 mm) and almost infinitely rigid (Young's modulus $E = 10^{15}$ N mm^{-2}) layer was laid on the whole section at both ends (Fig. 5b); for free warping, two different models were adopted. In one case, to match the actual experimental conditions (web in contact, flanges free), the rigid layers were placed only on the cruciform web, leaving the flanges free to warp (Fig. 5c). In the other case, to match the constraint condition of the one-dimensional model in our *in-house* code, the warping of the entire end sections was left free. All the constraints in the numerical models are bilateral. To end with, an amount of 3,680 and 14,720 elements were used to mesh the beam in the restrained and free warping conditions, respectively. The number of elements was increased so much in the latter case with respect to the former in order to describe warping of the end sections very accurately. Linear buckling and linear dynamic analyses were then run on each model to give the buckling load and the natural frequencies of the unloaded beam, respectively.

4.2. In-house finite difference code

The model in [4–10], direct, one-dimensional, based on Timoshenko theory of beams with shearing deformation, is enriched with a coarse descriptor of warping and describes kinematics with respect to the two parallel axes of the centres of area and shear. Finite kinematics yields linearised measures of strain pulled back to the reference configuration, fundamental in the investigations on elastic buckling. The scalar descriptor of warping is a new state parameter: it is not, in principle, a displacement at a point, but a measure of how the cross-section has come out of its original plane. Thus, the constraints of literature [1–3] between the warping rigidity and the twist are introduced, and the usual balance equations of force and couple, plus the auxiliary equation for the bi-shear and the bi-moment, are found in a straightforward way from the standard balance of power (virtual work), plus localization and regularity arguments. Non-linear hyper-elastic constitutive relations reflect known results of the literature, and make it possible to study perturbations of non-trivial equilibrium paths, and examine their stability by standard Ljapounov criteria; further information on the model and on its derivation can be found in [4–10], and, in particular, the details on the governing equations adopted here are well described in [8] (Section 2) and summarized in Appendix A of this paper.

Closed-form solutions, not usually at ease, are searched by an *in-house* numerical code based on [37]. Balance, compatibility, and constitutive equations, plus boundary conditions, are written in terms of finite differences, and their numerical solution is searched for; then, its stability is analyzed. The finite difference scheme is a central one, in which all derivatives (e.g., f') are rewritten as

$$\frac{f_{n+1}-f_n}{\Delta L_n}, \quad n = 1, 2, \ldots N \tag{1}$$

while all other unknowns and quantities (e.g., g) are expressed as

$$\frac{g_{n+1}+g_n}{2}, \quad n = 1, 2, \ldots N \tag{2}$$

f_n and g_n being the nodal values of the two generic functions f and g, ΔL_n the distance between two nodes (the length of an interval) and N the total number of intervals. Since the model is non-linear, a non-linear solver is adopted in order to find the equilibrium paths for the considered beam. If we wish to check their stability, the governing equations and the relevant boundary conditions are

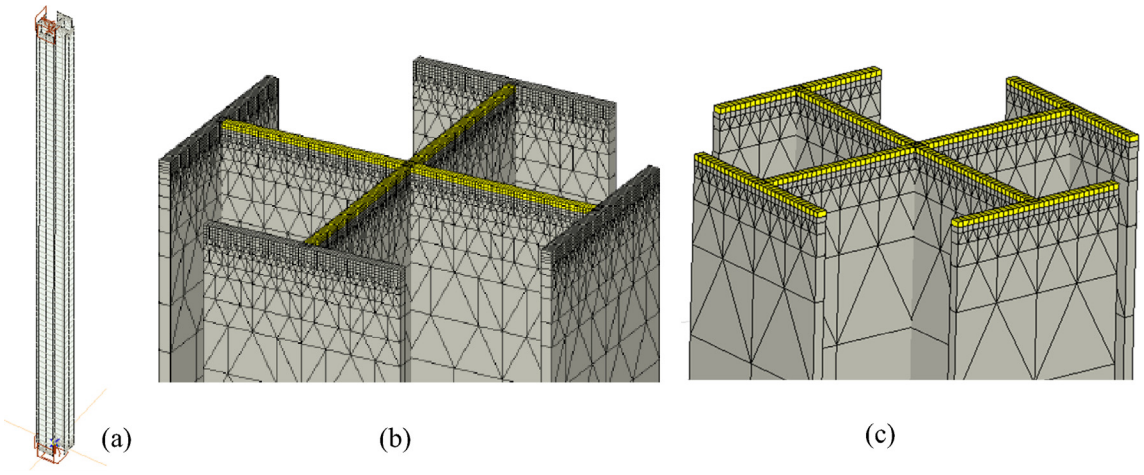

Fig. 5. Finite element models: (a) whole beam; detail of the mesh near the end for (b) free and (c) restrained warping condition.

linearised around the known equilibrium configurations, yielding a non-standard eigenvalue problem

$$[C]\{dX/dt^*\} = [B]\{X^*\} \tag{3}$$

where $\{X^*\}$ is a small perturbation of the beam equilibrium $\{X\}$, ruled by the matrices $[C]$ and $[B]$. The stability of the beam is described by the solutions of Eq. (3) of the kind

$$\{X^*\} = \{X_0^*\}e^{\lambda t} \tag{4}$$

The imaginary parts of the eigenvalues λ are the free vibration frequencies around the equilibrium configuration. Hence, when all eigenvalues have negative real part, equilibrium is stable; if an eigenvalue is real and positive, or has a real positive part, buckling or flutter occurs, respectively.

Thus, the main features of the model and of the relevant code are: (a) the beam model is direct, one-dimensional, Timoshenko-like, and enriched with a coarse descriptor of warping; (b) kinematics is finite, cross-sections are generic, and the constitutive relations are non-linear; (c) both conservative and non-conservative loadings can be considered; (d) the solution of the discretized field equations provides the equilibrium paths and their stability characters, accounting for the effect of the non-trivial configurations.

It is worth stressing that the model can detect both static (buckling) and dynamic (flutter) instabilities, yet always for the whole beam. Thus, the code can analyze *global* instabilities, and not local modes of the walls. Although this phenomenon can be significant for some peculiar applications, from a technical standpoint the slenderness ratios of the walls are usually designed so that local modes can be neglected.

In presence of warping, the normal stresses on the cross-section induce additional contributions to inner couples. This phenomenon can be non-linear, known as *second-order Wagner effect* [38,39]; since it is one order higher in strain measures than the already considered ones, it is neglected in the model; it becomes important at large twist rotations. On the other hand, the *first-order Wagner effect* [38,39] (after Wagner's pioneering work [40]), directly responsible of torsion buckling of compressed thin-walled members, is automatically considered by the model. In fact, the eigenvalue problem (3) well represents the linearisation of the overall perturbed governing equations, where the reduction of the effective torsion rigidity induced by the compressive force is included. More precisely, the adopted constitutive equations show that the inner torque does not depend only on the twist but also on the axial strain (see Appendix A); compressive stresses produce a torque which increases the twisting [38–40].

The code has been validated through comparisons with some paradigmatic (both analytical and numerical) solutions available in the literature: in [7], for beams with vanishing warping subjected to conservative and non-conservative loadings; in [8], for beams with non-zero warping subjected to conservative loadings; in [9], for beams with non-zero warping subjected to non-conservative loadings.

To implement the procedure, the values of length L, Young's modulus E, Poisson's ratio ν (whence the tangential modulus $G = E/[2(1+\nu)] = 26.54 \times 10^9$ N m^{-2}), density ρ, plus section properties are needed. From Table 1, in a central principal Cartesian system $\{O,x_1,x_2,x_3\}$, Table 3 lists the values of the section properties, following the notation in [4–10]: A, A_j are the area and the shear shape modified areas; A_{ij} are the mixed shear shape modified areas; J is the Saint-Venant torsion inertia factor; I_c is the polar moment of inertia with respect to the shear centre; I_j are the central principal moments of inertia; x_{cj} are the coordinates of the shear centre; I_{fj} are the flexural-torsion constants, and Γ is the cross-section warping constant ($i, j = 2, 3$). Since the cross-section is doubly symmetric, the mixed shear shape modified areas, the coordinates of the shear centre and the flexural-torsion constants vanish, i.e., $A_{ij} = x_{cj} = I_{fj} = 0$.

5. Results and comparisons

Fig. 6 shows the buckled shape of the beam in the monotonic compression test (i) performed in the free warping condition, and the corresponding first buckling mode given by FEM. Fig. 6a

Table 3
Sectional properties of the specimens.

A (mm^2)	$A_2 = A_3$ (mm^2)	$A_{23} = A_{32}$ (mm^2)	J (mm^4)	I_c (mm^4)	$I_2 = I_3$ (mm^4)	$x_{c2} = x_{c3}$ (mm)	$I_{f2} = I_{f3}$ (mm^5)	Γ (mm^6)
251.84	110.38	0	148.36	111,028	55,514	0	0	4,305,656

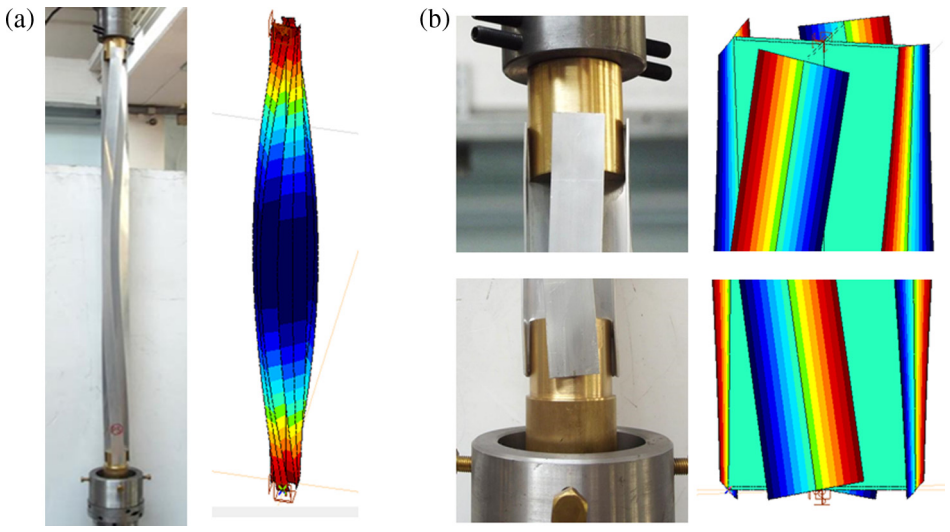

Fig. 6. Instability of the beam in the free warping condition: (a) torsion buckling mode, (b) detail of warping of the end sections.

shows that the beam buckles in torsion, i.e., the cross-sections rotate around the beam axis, which remains straight; the maximum rotation is attained at mid-length. During the test, the beam was pushed, in the post-critical range, until large rotations took place; consequently, plastic deformations were induced. Fig. 6b shows the detail of the warping deformation of the end sections corresponding to large post-critical rotations.

Fig. 7a shows the results of the displacement-controlled monotonic compression tests for the free and semi-restrained warping conditions, respectively. The curves show an initial settling, then a linear phase, and in the end a non-linear branch, reflecting the progressive degradation of the apparent beam stiffness. The load providing the end of the linear range, i.e., corresponding to the first evident stiffness reduction can be assumed as critical. Indeed, that point also corresponds to the occurrence of torsion rotations, which were almost absent before. The experimental critical load is then about 16 kN, while the values given by FEM are 16.5 kN for fully free warping, and 17.7 kN when only the flanges were free to warp.

Fig. 8 shows the buckled shape of the beam in the test (i) performed by restraining warping. Fig. 8a shows a global deformation similar to the previous one; the difference is in the strain of the end sections, see Fig. 8b: no warping occurs. The bottom left picture of Fig. 8b shows the (plastic) local buckling of the flanges, due to the restrained warping, after large post-buckling rotations. The top left picture of the same figure (which applies to both free and restrained warping) shows a top view of the plastic post-buckling twisted configuration. In this case, the experimental and numerical critical loads equal about 22 kN (derived from Fig. 7b, using the same criterion adopted for free warping) and 38.4 kN, respectively. However, while warping was totally restrained in FEM, the experimental constraint was closer to semi-restrained warping, as pointed out before; the latter constraint configuration was investigated by the finite difference *in-house* code, and will be discussed later on. If compared to the free warping condition, the critical load is increased by about 13% in the experiments (semi-restrained warping), and by about 22% in the numerical case (fully restrained warping).

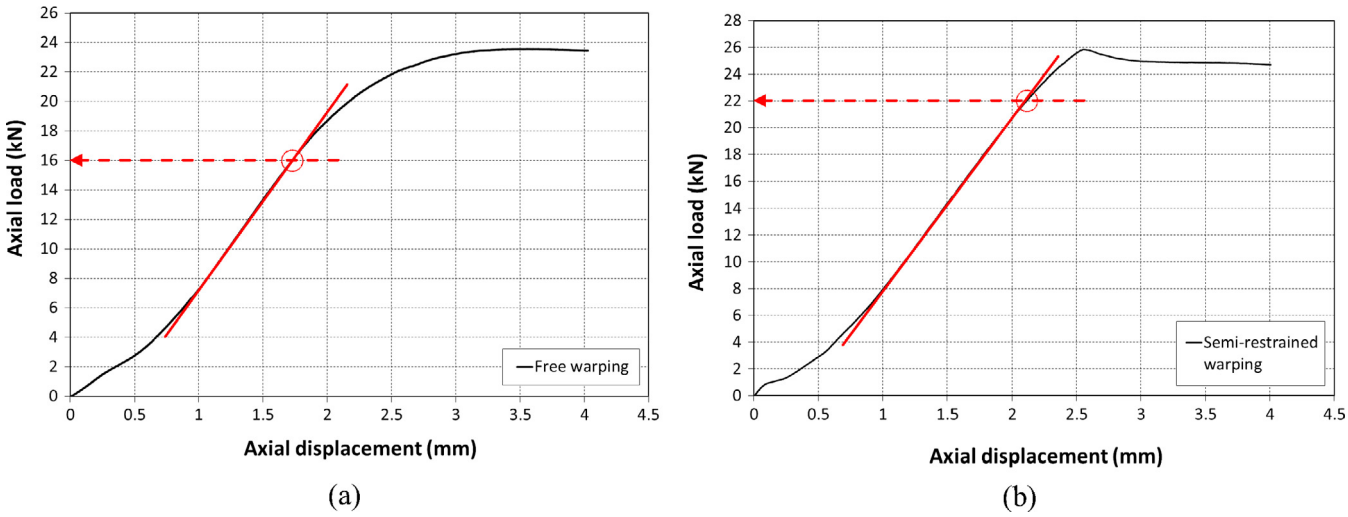

Fig. 7. Graphs of the curves of the experimental axial load (output) versus the axial displacement (input) for: (a) free warping, and (b) semi-restrained warping.

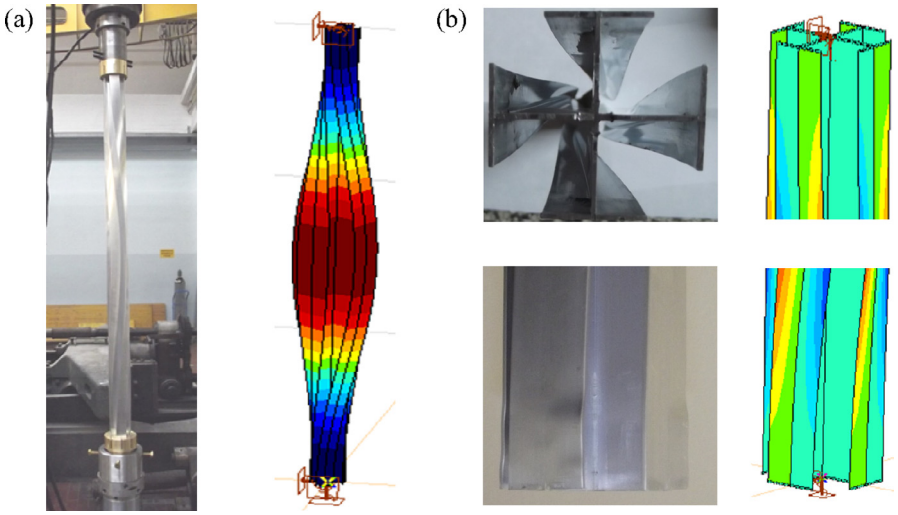

Fig. 8. Instability of the beam in the partially (experiments) and fully (FE models) restrained warping condition: (a) torsion buckling mode, (b) detail of the end sections and top view of the plastic post-buckling twisted configuration; notice (*bottom left*) the (plastic) local buckling of the flanges due to the restriction of warping, after large post-buckling rotations.

The length of the axis and the dimensions of the cross-section of the beam were chosen so that only global but no local and/or distortional buckling (i.e., in-plane deformation of the cross-sections) arises, as shown in Figs. 6a and 8a. Local and/or distortional buckling may occur in very thin-walled profiles, i.e., beams having webs and/or flanges with very high length-to-thickness ratios. Checks against local and distortional buckling were done, for both constraint conditions, by the software CUFSM 4.05 [41]. This employs a semi-analytical finite strip method, yielding solutions for the cross-section stability and elastic buckling analysis of thin-walled members with general end boundary conditions [42].

Fig. 9 shows the second buckling modes given by FEM in the case of free and restrained warping, respectively. Both are skew-symmetric torsion modes, with a node at mid-length, the only difference being represented by the end strain. The buckling loads are 41.1 kN and 68.7 kN, respectively; the former value occurs if the flanges are free to warp, as shown in Fig. 5c. These modes were not investigated experimentally (e.g., by preventing the torsion rotation of the central section). However, the numerical characterization of the second buckling mode will be useful afterwards for some remarks.

The variation of natural frequencies with the axial displacement/load was also investigated. As it is well known, warping has a great influence on the dynamics of thin-walled beams with open cross-section, especially for torsion vibration [43,44]. A preliminary modal analysis was performed in Axis VM 12 for the unloaded beam. Fig. 10 shows the first three stress-free vibration modes for both the analyzed end boundary conditions. In both cases, the first mode shows torsion, the second one shows bending in one principal plane of inertia (and is repeated twice because of the symmetry), while the third mode is again in torsion, but this time with a node at mid-length. Note that the second vibration mode is of bending, whereas the second buckling mode is a torsion one, with a central node (compare Figs. 9 and 10); however, the former is an actual vibration mode, while the latter is only virtual, unless suitable additional constraints are provided to the beam. The vibration frequencies corresponding to these modes are reported in the same Fig. 10. As one could have expected, restraining the end warping produces an increase in the natural frequencies: the first increases of about 70%, the second of about 12%, and the third of about 44%; it is interesting noting that the increase in the second frequency (bending mode) is lower than that for the other two frequencies, which correspond to torsion modes.

In principle, frequency-load interaction curves can be used for the non-destructive prediction of buckling loads [20,25–28]. In

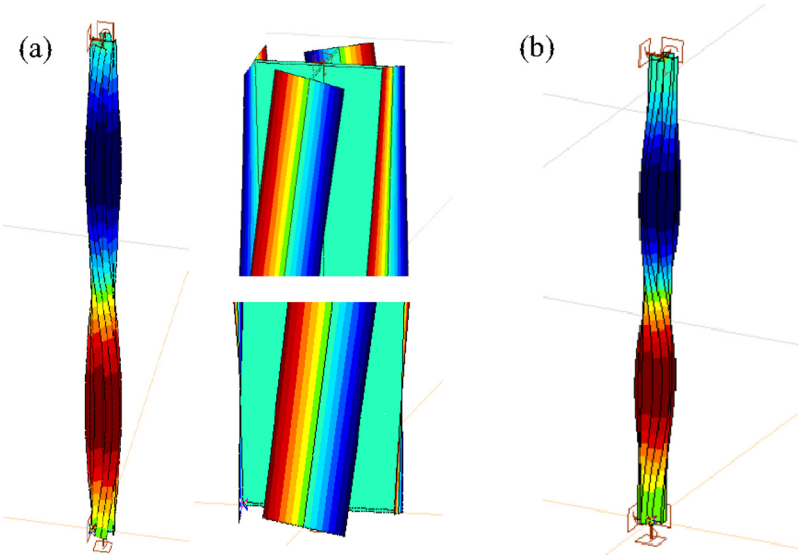

Fig. 9. Second FEM buckling mode for: (a) free warping, and (b) restrained warping.

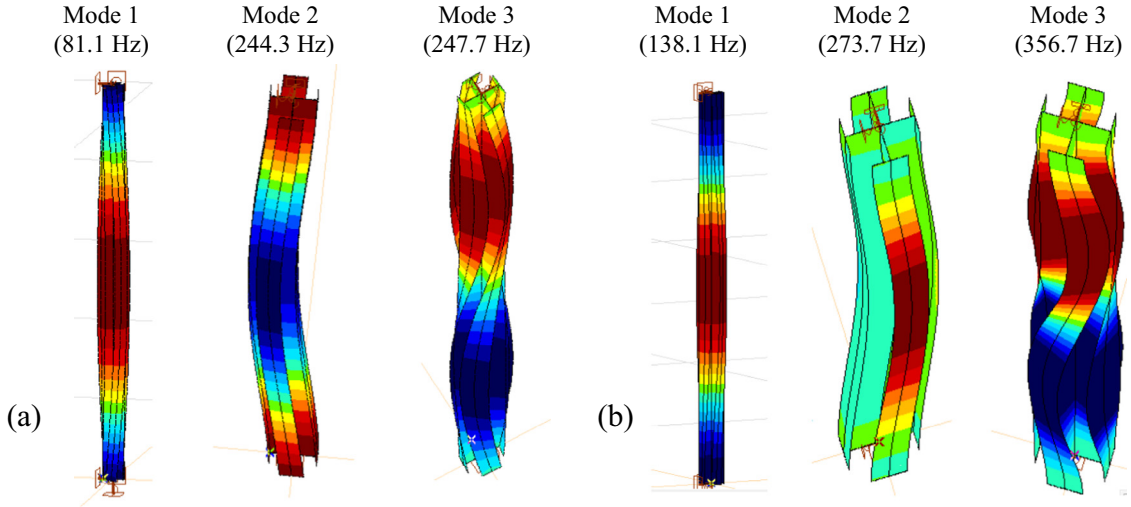

Fig. 10. First three FEM vibration frequencies and modes of the unloaded beam for: (a) free warping, and (b) restrained warping.

perfect (ideal) systems, the natural frequencies decrease with the compressive load, and vanish in correspondence of buckling loads [13–20]. Moreover, the dependence of the square of the frequency on the load is, in most of cases, linear or quasi-linear for static buckling. This enables us to predict buckling load by extrapolation of frequency values measured in correspondence of some loading levels, even far from the critical load [20,26]. In real systems, geometrical imperfections (e.g., initial curvature) or eccentric loads perturb the equilibrium path. Both the bifurcation point and the vanishing of natural frequencies disappear and, at least for small initial imperfections, the frequency-load curve exhibits a minimum near the buckling load of the corresponding perfect system [11,20,26]. Furthermore, the axial boundary condition has, in general, a large influence; i.e., passing from a statically determinate axial condition (e.g., pin-roller) to a statically indeterminate one (e.g. pin-pin) produces a change in the frequency-load interaction curve [11,21–24,45,46].

Fig. 11 collects the results of the dynamic tests (ii), showing the first three experimental frequency-load paths for the beams in both constraint conditions. Each frequency value represents the average of all the experimental values extracted by analyzing the measured signals. The first frequency is of a torsion mode, the second one is of a bending mode (repeated twice because of symmetry), and the third one is of a torsion mode with a central node (compare with Fig. 10c). The variation of natural frequencies with the load is always non-trivial. In general, they decrease as the load increases, but it is not always so, see Fig. 11. Indeed, the first and third frequencies (torsion) decrease down to a minimum, then increase again; on the other hand, the second frequency (bending) remains almost constant but from the very last part, where a tendency to increase emerges. Remark that the load always increases when the warping is free; on the other hand, for semi-restrained warping the axial load starts decreasing after the minimum of frequency. This denotes an unstable softening behaviour (recall that the test was conducted in a displacement controlled mode). Such complex frequency variations are not easy to predict, because of inevitable initial imperfections that usually have a remarkable effect.

The most important natural frequencies for elastic stability are the fundamental ones, governing the critical buckling mode and load. Fig. 12a compares the experimental fundamental frequencies for both analyzed configurations: they decrease with the axial load,

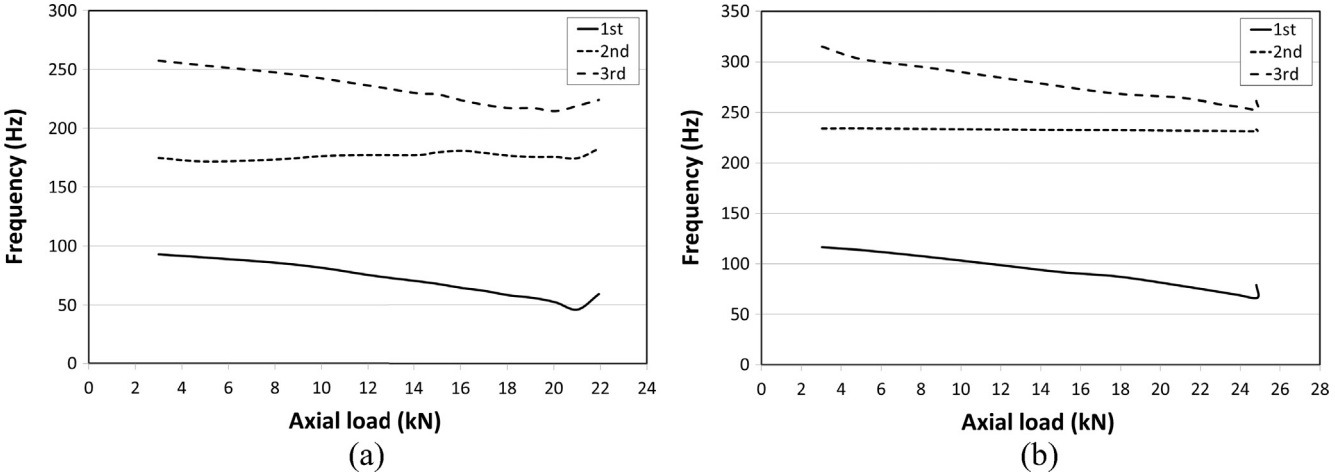

Fig. 11. Experimental frequency-load paths (axial displacement imposed) for: (a) free warping, and (b) semi-restrained warping.

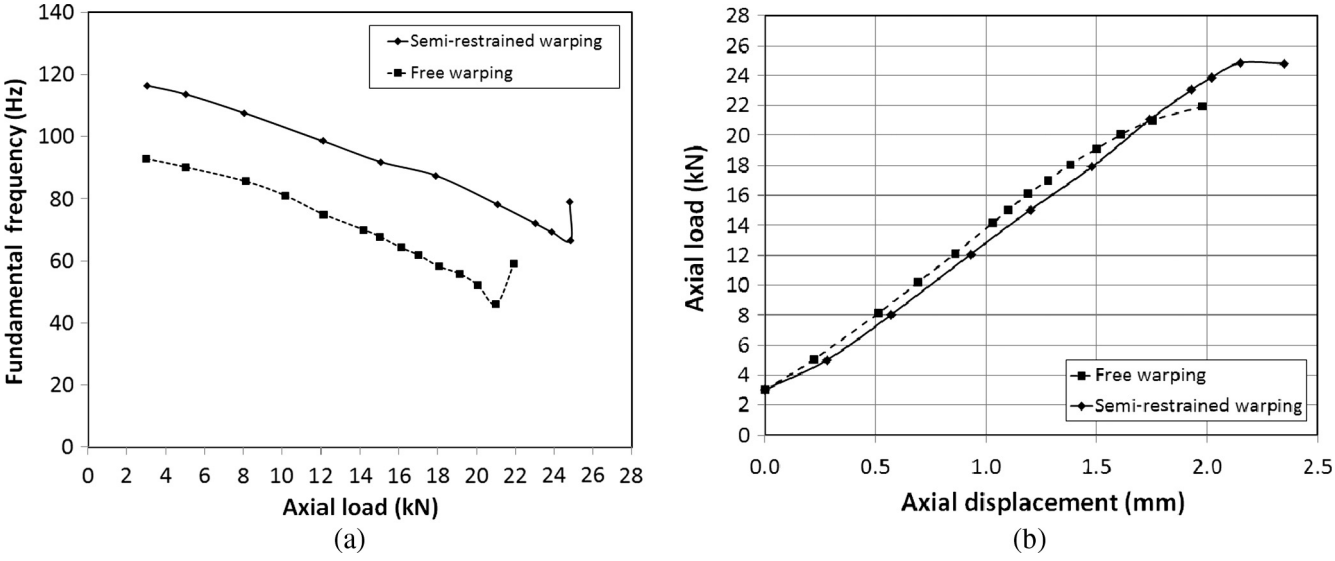

Fig. 12. Experimental (a) fundamental frequency vs. axial load and (b) axial load vs. axial displacement curves: comparison among free and semi-restrained warping.

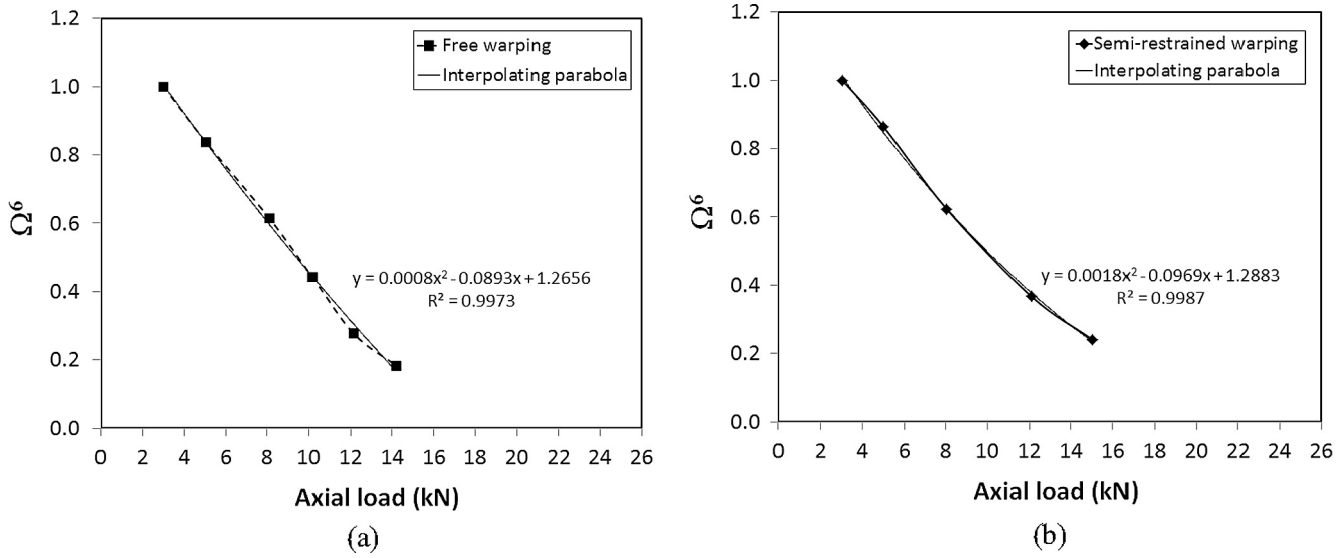

Fig. 13. Buckling load prediction from measured experimental frequencies according to the procedure in [26] for: (a) free warping and (b) semi-restrained warping.

but never vanish, either near or after the critical load, just as we pointed out before. This behaviour is typical of imperfect beams subjected to impressed axial end displacements [11,20–24]. The fundamental frequency falls by 50% in case of free warping, and by 25% for semi-restrained warping (percentage difference between the initial value and the minimum in the curve). In general, Fig. 12a shows that the introduction of end warping constraints increases both the frequency and the critical load. The load corresponding to the minimum of the fundamental frequency should correspond to the buckling load, or, more precisely, to the occurrence of large torsion rotations in this case. This happens when the load is about 21 kN and 25 kN for the free and semi-restrained warping conditions, respectively (see Fig. 12a). Actually, in the experiments torsion rotations were already observed before those values, i.e., buckling occurred for smaller compressive forces. As a confirmation Fig. 12b shows the axial load vs. axial displacement curves obtained by increasing the imposed displacement step-by-step (tests (ii)), not continuously as in test (i) (see Fig. 7).

A better estimate of the critical load was therefore obtained by applying the procedure suggested in [26]. This requires plotting the quantity Ω^{α} vs. the axial load and extrapolating the zero-crossing point from the initial values, $\Omega = \omega/\omega_0$ being the ratio of the natural frequencies ω, ω_0 corresponding to a generic and to the lowest load level, respectively; α is a natural number. The curve Ω^{α} vs. the axial load tends to switch from concave to convex as α is increased. This property may be used to predict lower and upper bounds for the buckling load starting from measured frequencies at low load levels. Indeed, as a general result of the stability theory, the first part of the frequency-load curve is less affected from initial imperfections and boundary conditions effects. Fig. 13 shows the result of this procedure, obtained using the first six (Fig. 13a) and the first five (Fig. 13b) frequency values for the free and the semi-restrained warping conditions, respectively. In both cases, after some trials, we set $\alpha = 6$ and interpolated data with a quadratic polynomial. The smallest root of the interpolating parabola gives a critical load of 16.7 kN for the free warping case and of 24.0 kN for semi-restrained warping.

In other words, if the buckling loads are estimated by looking at the minimum of the fundamental frequency-load curves (test (ii)), the values obtained (21 kN for free warping, 25 kN for semi-restrained warping) are quite far from the test (i) of monotonic compression (providing 16 kN for free warping and 22 kN for semi-restrained warping). Conversely, when buckling is evaluated processing the fundamental frequency-load curves with a more accurate scheme (like the extrapolation method in [26], from which a load of 16.7 kN for free warping and of 24 kN for semi-restrained warping) critical loadings are in good agreement with the test (i).

The results obtained by the *in-house* code, dividing the beam axis into 40 elements (41 nodes), are shown in Fig. 14: the curves fundamental frequency/axial load are compared for three end conditions (free, semi-restrained, and restrained warping). The axial end conditions were a fixed and a sliding support, while all the remaining degrees of freedom were restrained, with the exception of warping that was specified to reproduce each case. A peculiarity of the code is the simplicity and effectiveness for simulating semi-restrained warping: to this aim, it is sufficient to consider half the value of the warping constant of the actual cross-section, and then run the code as for fully restrained warping condition. In order to numerically detect the buckling load, the compression force is increased from zero to the critical condition, i.e., the vanishing of the fundamental frequency. Fig. 14 clearly highlights the critical compressive load for the three cases: 16.5 kN, for free warping conditions, 24.0 kN, for half-restrained warping conditions, and 38.6 kN, for restrained warping conditions. Since the fundamental

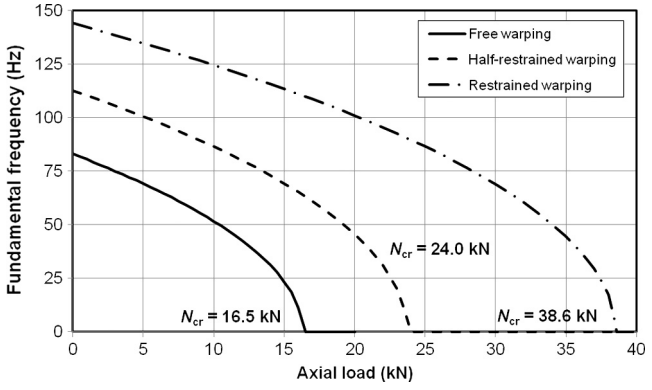

Fig. 14. Numerical (*in-house* code) fundamental frequency versus axial load curves (perfect beam, load imposed): comparison among free, half-restrained, and restrained warping conditions.

frequency is associated to a torsion mode, when it becomes zero the beam has lost its stiffness with respect to that motion, and, if perturbed, twists as shown before.

All experimental and numerical values of the buckling load obtained for all the analyzed configurations are collected in Table 4. We see that the numerical values of the *in-house* code are in good agreement both with the experimental results and those given by the finite element commercial code. It is useful to emphasize that the in house code allowed to reproducing the actual experimental conditions of semi-restrained warping in a truly simple and straightforward way. Nevertheless, the experimental and numerical frequency-load curves (Figs. 12a and 14) are quite different: this is because the numerical calculations were referred to a perfect beam, while the relevant experiment refers, of course, to a real (imperfect) beam. Such disagreements between laboratory and numerical conditions produced the aforesaid discrepancies, and justifies, for the real beam, the adoption of an extrapolation method able to detect the first critical load, that is the main design parameter in stability analysis.

As a further comparison, the analytical solution in the literature for torsion buckling is [2,47]:

$$N_{cr} = \frac{A}{I_c}\left[GJ + \left(\frac{\pi}{l}\right)^2 E\Gamma\right] \tag{5}$$

where l equals the length L for free warping, and $L/2$ for restrained warping; the other quantities were already described in Section 4.2. Eq. (5), with the values of Tables 1 and 3, provides a critical load of 16.3 kN for free warping and 38.4 kN for restrained warping, very close to those in Table 4. Comparing these values with the relevant numerical ones provided by the *in-house* code reveals that the latter are slightly greater than the analytical counterparts: this is likely because the code considers the effect of the non-trivial path and hence the shortening of the beam length because of the axial strain. It results that including the axial deformation in the buckling analysis slightly increases the stability limit.

It must be remarked that, while the *in-house* code applies to general problems (see Section 4.2 and Appendix A), the solution (5) holds for doubly symmetric sections, neglecting the non-trivial pre-critical equilibrium path and non-linear contributions. Analytical solutions also exist for the buckling of thin-walled beams without, or with only one, axis of symmetry [1,2,20,47]; however, they usually neglect the effect of pre-critical equilibrium paths, since they are obtained linearising the problem about the initial non-deformed configuration. In the case analyzed here, the cross-section is doubly symmetric, the beam axis is straight, and the compressive force is perfectly centred, thus the only possible pre-critical strain is the axial shortening. As we pointed out before, its effect on the buckling load is rather small. Conversely, the pre-critical equilibrium path may be relevant for thin-walled beams with non-symmetric cross-sections and/or subjected to eccentric compressive forces or bending moment/transverse loading. For all those cases, the *in-house* code capabilities are even more evident than for the present case [8,9]. Future comparisons with experimental results are planned for more general problems.

Table 5 shows a comparison in terms of the first natural frequency obtained experimentally and numerically for the unloaded beams in all the analyzed end conditions (in truth, for the experimental tests, the state of unloaded beam refers to a 'small' load of 3 kN necessary to remove the clearings in joints). The results confirm the general good agreement already revealed in terms of the critical loads (see Table 4), although in this case the experimental results point out values of frequencies quite larger than the numerical ones. This is mainly due to phenomena related to the friction in the joints; in fact, the case with semi-restrained warping has a smaller discrepancy than the free warping case (for which the permitted motion is certainly greater than in the former case).

As for the buckling loads, also the natural frequencies can be compared with the analytical solution; for example, the fundamental frequency of a torsion mode for an unloaded doubly symmetric beam free to warp is equal to [20]:

$$f_0 = \frac{1}{2L}\sqrt{\frac{E\Gamma(\pi/L)^2 + GJ}{\rho I_c}} \tag{6}$$

where all the quantities were already described in Section 4.2. By the data in Tables 1 and 3, Eq. (6) gives a frequency of 83.0 Hz, a value that practically coincides with the FDM prediction; both these values are slightly higher than that given by the FEM analysis (see Table 5).

Aiming to compare also the frequency-load path, the following dimensionless relation among the fundamental natural frequency and the axial load is adopted [20]:

$$\left(\frac{f}{f_0}\right)^2 = 1 - \frac{N}{N_{cr}} \tag{7}$$

that is, a linear relation between the normalized axial load N and the square of the normalized natural frequencies f; the critical load N_{cr} and the initial frequency f_0 have the values provided by Eqs. (5) and (6), respectively. Fig. 15 shows a comparison of the fundamental frequency versus axial load curves for the free warping conditions: the numerical path is practically overlapped to the analytical one; a small difference between the two graphs can be detected near the critical load, where the numerical code presents a slight stiffening effect due to considering the axial strain, as pointed out before. In other words, for the analyzed case, the *in-house* numerical code furnishes practically the same results given by the analytic solution. However, as already pointed out before, its use becomes very interesting in all those cases when closed form solutions are not available.

6. Final remarks

By means of a universal testing machine (MTS) and piezoelectric pickups, we investigated the frequency-load paths in compressed thin-walled beams with a double I symmetric section. After developing a suitable experimental setup, we were able to test the specimens under two different axial constraint conditions, i.e., free and partially restrained warping of the end sections. The specimens, clamped at both ends in flexure and torsion by suitably

Table 4
Comparison among experimental and numerical critical loads for different constraint conditions.

Case	N_{cr} Exp. (kN)	N_{cr} FEM (kN)	N_{cr} FDM (kN)
Free warping	16–16.7	16.5[a], 17.7[b]	16.5
Semi-restrained warping	22–24.0	–	24.0
Fully restrained warping	–	38.4	38.6

[a] Centroid restrained.
[b] Web restrained.

Table 5
Comparison among experimental and numerical fundamental frequencies for the different constraint conditions.

Case	Exp.[a] (Hz)	FEM[b] (Hz)	FDM[b] (Hz)
Free warping	92.9	81.1	83.1
Semi-restrained warping	116.5	–	112.7
Fully restrained warping	–	138.1	144.1

[a] Beam under a compressive load of 3 kN.
[b] Unloaded beam.

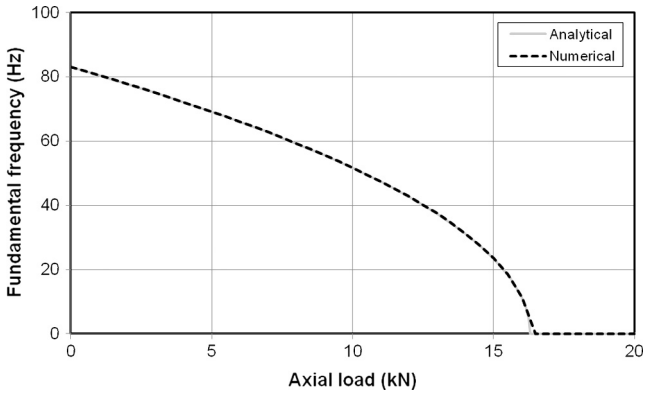

Fig. 15. Numerical (*in-house* code) and analytical fundamental frequency versus axial load curves for free warping conditions.

designed and manufactured devices, were therefore subjected to increasing compressive axial displacements up to the post-buckling condition. Thus, the effects of warping rigidity on both natural frequencies and buckling loads were investigated.

The tested profiles were such that elastic instability occurred by torsion buckling (the fundamental vibration was of torsion). For such profiles the great contribution to torsion stiffness is due to warping rigidity, since Saint-Venant's torsion rigidity is negligible. The experimental results reveal a large influence of warping and warping constraints on natural frequencies and buckling loads for the analyzed thin-walled profiles. In particular, the restriction of warping deformation of the end sections increases both natural frequencies and buckling loads.

The experimental results were compared, in terms of critical loads and natural frequencies, with those obtained by numerical simulations. In detail, we implemented finite element models in a commercial code, and performed numerical computations using an *in-house* code based on a finite difference procedure. The latter adopts a Timoshenko-like beam model enriched with a new scalar parameter describing the average warping of the cross-sections. All the numerical results regarding stability are in agreement to each other, as well as to the experimental findings. Comparisons were also made with respect to analytical and/or closed-form solutions of literature. This represents a validation of our *in-house* code for the prediction of the buckling load. The main advantages with respect to finite element shell models are: (a) the high accuracy compared to the small computational cost (relatively small number of subdivisions versus the large number of nodes/elements typical of finite element shell models); (b) the easy and fast introduction of input data required to create/modify a full model; (c) the possibility to investigate, in an easy and rapid way, even non-conventional boundary conditions, like that of a semi-restrained warping, which is not of immediate implementation in a finite element model; and (d), most importantly, the possibility to take into account, by default, the influence of non-trivial pre-critical equilibrium paths in elastic stability analysis. By contrast, shell (and solid) models make it possible to investigate also local buckling and/or in-plane cross-section distortions. Such deformations, typical of beams with extremely thin walls, cannot be described with ordinary 1-D reduced models; higher-order beam theories must be adopted, see for example [48]. However, none of the latter two phenomena took place in the analyzed beams, the walls of which were not thin enough. For this reason, that problem is beyond the scope of the present study. Moreover, in general, shell and solid models also allow a more accurate prediction of the natural vibration frequencies, as they permit closer reproductions of the actual mass distribution. However, for thin walled beams, 1-D models often give satisfactory results with very low computational cost and modelling time.

A final comment must be reserved to the obtained frequency-load curves. The experimental results clearly show that static instability (buckling) may occur at a fundamental frequency other than zero. Actually, the zero-frequency condition in correspondence of the critical load is attained only in perfect systems, where a bifurcation of the equilibrium path occurs. Conversely, in real systems, where several initial imperfections are present, the pre-critical equilibrium path shows a progressive reduction of the stiffness with respect to a deformation mode, eventually followed by a stiffness recovery in the case of systems exhibiting a stable post-critical branch. This variation of structural stiffness with the axial load is reflected in the frequency-load paths, where the fundamental frequency decreases to a minimum (near the critical load) as the compression load is increased; afterwards, it may start increasing again with the load when the post-critical path is stable. Moreover, the effect of the axial boundary condition (e.g., pinned-roller vs. pinned-pinned supports) also has a great influence on the frequency-load curve. This behaviour has been observed and investigated for slender beams with compact cross-sections by several researchers, included some of the authors [11,21–24,45,46]. These last fundamental aspects must be well taken into account, for example, when monitoring the stability of in-service structural elements and components by measuring their fundamental frequency. In this case, refer to the zero-frequency condition as an indicator of instability may induce a dangerous overestimate of the stability limit. Also referring to the minimum of fundamental frequency may not be safe, as we showed in this paper; thus, specific procedures, like the ones suggested in [20,26], have to be applied to obtain buckling load predictions from measured frequency-load curves.

In general, it must be observed that initial geometrical imperfections have no influence on the critical load yield by second-order analyses [1,2]. This implies that the zero-frequency condition of classic frequency-load curves can still be used (in principle) to predict the critical load by means of analytical or numerical computations, like in our *in-house* code. At the same time, initial geometrical imperfections affect the actual equilibrium path, and therefore also affect the frequency-load curve.

Acknowledgements

The Authors gratefully acknowledge the company La Milano srl for the accurate realization of the specimens, in particular Mr. L. Bernasconi for his availability and competence. Special thanks are also due to Ind. Eng. F. Alasia for precious technical advices in designing and realizing the end joints, and to Engs. R. Malvano and M. Tonici for the needful cooperation provided in several phases of the present study. We also acknowledge the support of institutional grants of "La Sapienza" university, Rome, Italy.

Appendix A. Direct model for open thin-walled profiles

In the Euclidean ambient space, the beam has cylindrical reference shape $C_0 = S \times [0, l]$ consisting of cross-sections attached at their centroids o and shear centres c [4,49] to parallel axes of length l; thus, the vector $\mathbf{c} = c - o$ is uniform. The cross-sections are copies of a plane figure S, which is the regular thickening a plane arc, called middle line; any definition for c [50,51] works. A Cartesian frame has origin at the centroid of the left end of C_0; the x_1-axis is centroidal; x_2 and x_3 are principal axes of inertia of cross-sections. Another configuration C is described by the suitably regular: (a) vector position of the beam axes $\mathbf{p}_h = \mathbf{q}_h + \mathbf{u}_h$, $h = o, c$, given by the position of the same axes in C_0, plus the relevant

displacement; (b) tensor $\mathbf{R}$ of rotation of cross-sections; (c) scalar α of coarse description of the cross-sections warping. Thus, kinematics assumes rigid cross-sections, to which a descriptor of warping is superposed; this is not, in principle, the actual out-of-plane displacement of a place in S, but rather a measure of this phenomenon, which could be the value of the so-called sectorial area [3] at a chosen point, or an average of the so-called warping function [52].

In a rigid motion, cross-sections rotate uniformly with x_1; all vectors rotate accordingly; warping is nil. Observer-invariant strain measures pulled back to C_0 are rigidity defects, given by

$$\mathbf{E} = \mathbf{R}^T\mathbf{R}', \quad \mathbf{e}_h = \mathbf{R}^T\mathbf{p}_h' - \mathbf{q}_h', \quad h = o, c, \quad \alpha$$

where a prime denotes the x_1-derivative. The skew tensor $\mathbf{E}$ is the curvature of one of the beam axes in C. The vectors $\mathbf{e}_h$ are the differences of tangents to the axes (those in C pulled back to C_0 and those in C_0). In the basis $\{\mathbf{a}_1, \mathbf{a}_2, \mathbf{a}_3\}$ consistent with the chosen coordinates,

$$\mathbf{s} = \mathbf{R}^T\mathbf{s} = Q_m\mathbf{a}_m, \quad \mathbf{S} = \mathbf{R}^T\mathbf{S}\mathbf{R} = e_{mnp}S_m\mathbf{a}_n \otimes \mathbf{a}_p$$

are the contact forces and couples in C_0: Q_1 is the normal, Q_m, $m = 2, 3$, are the shearing forces; S_1 is the twisting, S_m, $m = 2, 3$, are the bending couples.

We can thus write P^i with the normal and the shearing forces applied at o and c, respectively

$$\begin{aligned} P^i &= \int_0^l (\mathbf{s}\cdot\dot{\mathbf{e}}_c + \mathbf{S}\cdot\dot{\mathbf{E}} + \tau\dot{\omega} + \mu\dot{\omega}')dx_1 \\ &= \int_0^l (Q_1\dot{\varepsilon}_{1o} + Q_2\dot{\varepsilon}_{2c} + Q_3\dot{\varepsilon}_{3c} + S_1\dot{\kappa}_1 + M_2\dot{\kappa}_2 + M_3\dot{\kappa}_3 + \tau\dot{\omega} \\ &\quad + \mu\dot{\omega}')dx_1 \end{aligned}$$

where the following sums of a couple and the moment of a force are bending torques reduced to o

$$M_2 = S_2 + x_{c3}Q_1, \quad M_3 = S_3 - x_{c2}Q_1$$

Thus, the scalar form of the local balance of force and torque is

$$\begin{aligned} &Q_1' + \kappa_2Q_3 - \kappa_3Q_2 = 0, \quad S_1' + \kappa_2M_3 - \kappa_3M_2 + (x_{c2}\kappa_2 + x_{c3}\kappa_3)Q_1 + \varepsilon_{2c}Q_3 - \varepsilon_{3c}Q_2 = 0, \\ &Q_2' + \kappa_3Q_1 - \kappa_1Q_3 = 0, \quad M_2' + \kappa_3S_1 - \kappa_1M_3 - x_{c3}Q_1' + (\varepsilon_{3c} - x_{c2}\kappa_1)Q_1 - (1 + \varepsilon_{1c})Q_3 = 0, \\ &Q_3' + \kappa_1Q_2 - \kappa_2Q_1 = 0, \quad M_3' + \kappa_1M_2 - \kappa_2S_1 + x_{c2}Q_1' - (\varepsilon_{2c} + x_{c3}\kappa_1)Q_1 + (1 + \varepsilon_{1c})Q_2 = 0. \end{aligned}$$

$$\mathbf{E} = e_{mnp}\kappa_m\mathbf{a}_n \otimes \mathbf{a}_p, \quad \mathbf{e}_h = \varepsilon_{mh}\mathbf{a}_m, \quad h = o, c; \quad m, n, p = 1, 2, 3$$

Here, e_{mnp} is Ricci's permutation operator; κ_1 is the twist, and κ_m, $m = 2, 3$ are the bending curvatures; ε_{1h} *is* the strain of the relevant axis; ε_{mh}, $m = 2, 3$ are the shearing strains between the cross-sections and the relevant axis. The strains with respect to o, c are related through

$$\begin{aligned} &\mathbf{e}_c = \mathbf{e}_o + \mathbf{E}\mathbf{c}, \quad \mathbf{c} = x_{c2}\mathbf{a}_2 + x_{c3}\mathbf{a}_3, \\ &\varepsilon_{1c} = \varepsilon_{1o} + x_{c3}\kappa_2 - x_{c2}\kappa_3, \quad \varepsilon_{2c} = \varepsilon_{2o} - x_{3c}\kappa_1, \quad \varepsilon_{3c} = \varepsilon_{3o} + x_{c2}\kappa_1 \end{aligned}$$

If $\mathbf{R}_1$ rotates of ϕ_1 about $\mathbf{a}_1$, $\mathbf{R}_2$ rotates of ϕ_2 about $\mathbf{R}_1\mathbf{a}_2$, and $\mathbf{R}_3$ rotates of ϕ_3 about $\mathbf{R}_2\mathbf{R}_1\mathbf{a}_3$, it is

$$\mathbf{R} = \mathbf{R}_3\mathbf{R}_2\mathbf{R}_1, \quad \mathbf{u}_h = \mathbf{p}_h - \mathbf{q}_h = u_{mh}\mathbf{a}_m, \quad h = o, c; \quad m = 1, 2, 3$$

and strains derive consequently [4,10,49].

The velocities are, a dot denoting time-derivative, the cross-section spin $\mathbf{W} = \dot{\mathbf{R}}\mathbf{R}^T$, the axes velocity $\dot{\mathbf{w}}_h = \dot{\mathbf{p}}_h$, and the warping ratio $\omega = \dot{\alpha}$. The external power P^e is a linear functional of test velocities in C, with respect to either c or o. Asking P^e to be observer-invariant yields the balance of global force and torque, reduced to either c or o: then, inertia and contact actions shall be constitutively prescribed.

If any point interacts only with those in its neighbourhood, the internal power P^i is linear in the test velocities and their first x_1-derivatives, and vanishes in any change of observer. For any test velocity and at any time, the balance of power holds: $P^i = P^e$. Then, localization yields the 'law of action and reaction'; the fundamental theorem of integral calculus, plus localization, yields

$$\mathbf{t}' + \mathbf{b} = \mathbf{0}, \quad \mathbf{T}' + \mathbf{p}_c \wedge \mathbf{t} + \mathbf{B} = \mathbf{0}, \quad \mu' - \tau + \beta = 0$$

The vector densities $\mathbf{b}$, $\mathbf{t}$ are bulk and surface forces, respectively; the skew tensor densities $\mathbf{B}$, $\mathbf{T}$ are bulk and surface couples, respectively; the scalar densities β, μ, τ are bulk and surface warping actions. These equations provide the local balance of force and torque reduced to c, plus the auxiliary equation for μ and τ, interpreted as bi-moment and bi-shear [2,3,52]. The auxiliary balance is configuration-independent, while it is not so for the balance of force and torque. The latter are pulled back to C_0, if

For homogeneous elastic beams, constitutive axioms [53] yield the material response. As for inner constraints, warping is postulated to depend on twist [2,3,52,54]: if ξ is a real constant (identified by refined models), this constraint reads

$$\alpha = \xi\kappa_1, \quad \alpha' = \xi\kappa_1'$$

and reacts spending no power on compatible motions. Inner forces, bending torques, and the bi-moment turn out to be only active; the reactive part of the twisting couple is linear in the bi-shear [3,4,10,49], which, by the auxiliary equation, is given in terms of the bi-moment if we search equilibria ($\beta = 0$).

A hyper-elastic potential shall describe usual couplings (see, e.g., second-order elasticity in [55,56], and Wagner's effect [38–40]). Expanding the potential up to the third order of the strain measures,

$$Q_1 = EA\varepsilon_{1o} + \frac{1}{2}EI_c\kappa_1^2, \quad Q_m = GA_{mn}\varepsilon_{nc}, \quad m, n = 2, 3, \quad \mu = \frac{E\Gamma}{\xi}\kappa_1',$$

$$S_1 = (GJ + EI_c\varepsilon_{1o} + EI_{f2}\kappa_2 - EI_{f3}\kappa_3)\kappa_1 - \xi\mu',$$

$$M_m = EI_m\kappa_m + \frac{1}{2}EI_{fm}\kappa_1^2, \quad m = 2, 3$$

with E, G Young's and shear moduli; A and A_{mn} the cross-section area and shear areas; J the Saint- Venant torsion factor; I_c the polar moment of inertia referred to c; I_m the central principal moments of inertia; I_{fm} the third-order moments of inertia; Γ the warping factor [2–4,8,10,49,52]. The second addends for the axial force and the twisting couple account for (first order) Wagner's effect, i.e., the coupling between the axial strain/stress of compression and the twist (recall that no constraint on elongation is posed). The second addend for the bending moments and the third and fourth addends for the twisting couple account for generalised Poynting-like couplings between bending strain/stresses and the twist.

Writing strains in terms of displacements yields the field equations. We find that ξ influences only warping, bi-shear and bi-moment, not the results. Thus, its value is immaterial, and, re-scaling bi-moment as $B = \xi\mu$ [54], field equations without

reactive terms are obtained: bi-shear and warping may be evaluated in a post-processing phase.

Field equations are linearised around C_0; inertial terms for warping are not discussed much in the literature, and in a direct 1-D model any reasonable hypothesis fits. By a kinematical identification with the 3-D model in [52] with the constraint between coarse warping and twist, if ρ is the beam mass density in C_0 we pose

$$\beta = \frac{\rho A \Gamma}{\xi} \ddot{\phi}_1$$

References

[1] Pignataro M, Rizzi N, Luongo A. Stability, bifurcation, and postcritical behaviour of elastic structures. Amsterdam: Elsevier; 1991.
[2] Timoshenko S, Gere JM. Theory of elastic stability. New York: McGraw-Hill; 1961.
[3] Vlasov VZ. Thin-walled elastic beams. Jerusalem: Monson; 1961.
[4] Ruta G, Pignataro M, Rizzi N. A direct one-dimensional beam model for the flexural-torsional buckling of thin-walled beams. J Mech Mater Struct 2006;1:1479–96.
[5] Ruta G, Pignataro M, Rizzi N. A beam model for the flexural-torsional buckling of thin-walled members. Thin-Walled Struct 2008;46:816–22.
[6] Pignataro M, Rizzi N, Ruta G, Varano V. The effects of warping constraints on the buckling of thin-walled structures. J Mech Mater Struct 2010;4:1711–27.
[7] Lofrano E, Paolone A, Ruta G. Stability of non-trivial equilibrium paths of beams on partial visco-elastic foundation. Acta Mech 2012;223:2183–95.
[8] Lofrano E, Paolone A, Ruta G. A numerical approach for the stability analysis of open thin-walled beams. Mech Res Commun 2013;48:76–86.
[9] Brunetti M, Lofrano E, Paolone A, Ruta G. Warping and Ljapounov stability of non-trivial equilibria of non-symmetric open thin-walled beams. Thin-Walled Struct 2015;86:76–86.
[10] Brunetti M, Paolone A, Ruta G. On inner shearing constraints for a direct beam model coarsely describing warping. Meccanica 2013;48:2439–51.
[11] Carpinteri A, Malvano R, Manuello A, Piana G. Fundamental frequency evolution in slender beams subjected to imposed axial displacements. J Sound Vib 2014;333:2390–403.
[12] Piana G, Manuello A, Malvano R, Carpinteri A. Fundamental frequencies of slender beams subject to imposed axial end displacements. In: Sottos N, Rowland R, Dannemann K, editors. Experimental and applied mechanics: proceedings of the 2014 annual conference on experimental and applied mechanics, conference proceedings of the society for experimental mechanics series, vol. 6; 2014.
[13] Massonnet C. The relations between the normal modes of vibration and stability of elastic systems. Bulletin des Cours et des Laboratoires D'Essais des Constructions du Génie Civil et d'Hydraulique Fluviale (Bulletin du C.E.R.E.S.) 1; 1940.
[14] Belluzzi O. On the vibration period of a structure in presence of compressive axial loads. Giornale del Genio Civile 1951;4 (in Italian).
[15] Lurie H. Lateral vibrations as related to structural stability. J Appl Mech 1952;19:195–204.
[16] Galef AE. Bending frequencies of compressed beams. J Acoust Soc Am 1968;44 (8):643.
[17] Bokaian A. Natural frequencies of beams under compressive axial loads. J Sound Vib 1988;126(1):49–65.
[18] Abramovich H. Natural frequencies of Timoshenko beams under compressive axial loads. J Sound Vib 1992;57(1):183–9.
[19] Matsunaga H. Free vibration and stability of thin elastic beams subjected to axial forces. J Sound Vib 1996;191(5):917–33.
[20] Virgin LN. Vibration of axially loaded structures. New York: Cambridge University Press; 2007.
[21] Dickinson SM. The lateral vibration of slightly bent slender beams subject to prescribed axial end displacement. J Sound Vib 1980;68(4):507–14.
[22] Kim CS, Dickinson SM. The flexural vibration of slightly curved slender beams subject to axial end displacement. J Sound Vib 1986;104(1):170–5.
[23] Yamaki N, Mori A. Non-linear vibrations of a clamped beam with initial deflection and initial axial displacement, Part I: theory. J Sound Vib 1980;71 (3):333–46.
[24] Ilanko S. The vibration behaviour of initially imperfect simply supported beams subject to axial loading. J Sound Vib 1990;142(2):355–9.
[25] Belluzzi O. On the experimental determination of the critical load through vibration tests. Ingegneri-Architetti-Costruttori 1951;4 (in Italian).
[26] Plaut RH, Virgin NL. Use of frequency data to predict buckling load. J Eng Mech 1990;116(10):2330–5.
[27] Anik'ev II, Mikhailova MI, Sushchenco EA. Nondestructive determination of the critical load of column-type structures. Int Appl Mech 1994;30(12):990–4.
[28] Anik'ev II, Sushchenko EA. Experimental nondestructive determination of critical loads on thin-walled structures. Int Appl Mech 2002;38(4):485–8.
[29] Lofrano E, Carpinteri A, Malvano R, Manuello A, Piana G, Ruta G. PZT experimental detection of natural frequencies for compressed thin-walled beams. In: SEM 2015 annual conference and exposition on experimental and applied mechanics, Costa Mesa, CA; June 8–11, 2015.
[30] Piana G, Brunetti M, Carpinteri A, Malvano R, Manuello A, Paolone A. On the use of piezoelectric sensors for experimental modal analysis. In: SEM 2015 annual conference and exposition on experimental and applied mechanics, Costa Mesa, CA; June 8–11, 2015.
[31] Piana G, Lofrano E, Carpinteri A, Paolone A, Ruta G. Experimental modal analysis of straight and curved slender beams by piezoelectric transducers. Meccanica 2016;51(11):2797–811.
[32] De Silva CW. Vibration. Fundamentals and practice. Boca Raton: CRC Press; 2000.
[33] Ewins DJ. Modal testing: theory, practice and application. 2nd ed. Baldock: Research Studies Press; 2000.
[34] Fu Z-F, He J. Modal analysis. Oxford: Butterworth-Heinemann; 2001.
[35] www.axisvm.eu.
[36] http://axisvm.eu/axisvm_download_manual.html.
[37] Hodges DH. Geometrically exact, intrinsic theory for dynamics of curved and twisted anisotropic beams. AIAA J 2003;41:1131–7.
[38] Trahair NS. Wagner's beam cycle. Research report R916. Sydney (Australia): School of Civil Engineering, The University of Sydney; March 2011. ISSN 1833-2781.
[39] Attard MA. Finite strain–beam theory. Int J Solids Struct 2003;40:4563–84.
[40] Wagner H. Verdrehung und Knickung von offenen Profilen (Torsion and buckling of open sections). In: 25th anniversary publication, Technische Hochschule, Danzig, 1904–1929, translated as Technical Memorandum No. 807. U.S. National Advisory Committee for Aeronautics; 1936.
[41] http://www.ce.jhu.edu/bschafer/cufsm/index.htm.
[42] Li Z, Schafer BW. Buckling analysis of cold-formed steel members with general boundary conditions using CUFSM: conventional and constrained finite strip methods. In: Proceedings of the 20th int. l spec. conf. on cold-formed steel structures, St. Louis, MO; November 2010.
[43] Aminbaghai M, Murin J, Hrabovsky J, Mang HA. Torsional warping eigenmodes including the effect of the secondary torsion moment on the deformations. Eng Struct 2016;106:299–316.
[44] Dikaros IC, Sapountzakis EJ, Argyridi AK. Generalized warping effect in the dynamic analysis of beams of arbitrary cross section. J Sound Vib 2016;369:119–46.
[45] Woinowsky-Krieger S. The effect of an axial force on the vibration of hinged bars. J Appl Mech 1950;17:35–6.
[46] Burgreen D. Free vibrations of a pin-ended column with constant distance between pin ends. J Appl Mech 1951;18:135–9.
[47] Bažant ZP, Cedolin L. Stability of structures – elastic, inelastic, fracture and damage theory. New York: Dover Publications; 2003.
[48] Carrera E, Giunta G, Petrolo M. Beam structures: classical and advanced theories. Wiley; 2011. ISBN 9780470972007.
[49] Pignataro M, Ruta G, Rizzi N, Varano V. Effects of warping constraints and lateral restraint on the buckling of thin-walled frames. ASME Int Mech Eng Congr Exposition Mech Syst Contr Parts A and B 2009;10:803–10.
[50] Andreaus UA, Ruta G. A review of the problem of the shear center(s). Continuum Mech Thermodyn 1998;10(6):369–80.
[51] Ruta G. On the flexure of a Saint-Venant cylinder. J Elast 1999;52(2):99–110.
[52] Simo JC, Vu-Quoc L. A geometrically exact rod model incorporating shear and torsion-warping deformation. Int J Solids Struct 1991;27(3):371–93.
[53] Truesdell C, Noll W. The non-linear field theories of mechanics. NewYork: Springer-Verlag; 1965.
[54] Møllmann H. Theory of thin-walled beams with finite displacements. Lect Notes Eng 1986;19:195–209.
[55] dell'Isola F, Ruta G, Batra R. Generalized Poynting's effects in predeformed prismatic bars. J Elast 1998;50(2):181–96.
[56] dell'Isola F, Ruta G, Batra R. A second-order solution of Saint-Venant's problem for anelastic bar predeformed in flexure. Int J Non-Linear Mech 2005;40(2–3):411–22.